Nanometric phonon spectroscopy for diamond and cubic boron nitride

Jun Kikkawa [1,2,*] Takashi Taniguchi,[3] and Koji Kimoto [1]

[1]*Research Center for Advanced Measurement and Characterization, National Institute for Materials Science,
1-1 Namiki, Tsukuba 305-0044, Japan*
[2]*JST, PRESTO, 4-1-8 Honcho, Kawaguchi 332-0012, Japan*
[3]*International Center for Materials Nanoarchitectonics, National Institute for Materials Science, 1-1 Namiki, Tsukuba 305-0044, Japan*

Local phonon properties near heterointerfaces or lattice defects are key for controlling various material properties such as thermal conductivity and thermoelectricity. However, high-spatial-resolution measurements of bulk phonons have hardly been established, even in typical nonpolar and polar bulk materials such as diamond and cubic boron nitride (c-BN), respectively. Here, we demonstrate nanometric measurements of phonon dispersions and mapping using a heterojunction of diamond and c-BN single crystals. To achieve high spatial/energy resolution, we use a monochromated ($\sim$20–30 meV) electron nanoprobe, a high-sensitivity scintillator for counting inelastically scattered electrons, and the Richardson–Lucy deconvolution. The diamond phonon dispersion is first measured under a large-scattering-vector condition, particularly for the Γ point. Differential scattering cross sections of optical and acoustic-phonon modes in diamond and c-BN are also measured, and the totals of their modes are on the order of 10^{-5} nm^2 for both crystals.

Introduction. Thermal properties of solids, such as thermal conductivity and heat capacity, are largely governed by phonons. Controlling phonon transport at nanometer scales is important to realize efficient heat dissipation in high-frequency and high-power devices with heterointerfaces and produce high-ZT thermoelectric materials. Introducing dissipation paths in materials with high thermal conductivity such as diamond promotes phonon transport [1–3], whereas introducing lattice defects increases phonon scattering and thus enhances ZT [4,5]. Therefore the measurement and understanding of phonon properties at heterointerfaces and lattice defects at nanometer scales are very important.

Recently, electron energy-loss spectroscopy (EELS) combined with scanning transmission electron microscopy (STEM) with energy resolutions of 5–30 meV has made it possible to detect phonons at the nanometer [6–8] and even atomic [9,10] scales. The spatial resolution Δx in STEM–EELS ($\Delta x \sim 10^{-2}$–10 nm) is advantageous over that of other tools for analyzing bulk phonons, i.e., inelastic neutron scattering ($\Delta x \sim 10^6$–10^8 nm) and inelastic x-ray scattering ($\Delta x \sim 10^4$–10^5 nm) [11]. Measurements of phonon dispersion [12,13] and temperature [14,15] at the nanometer scale are also feasible using STEM–EELS by probing the wave-vector dependence and energy gain/loss ratio of phonons. STEM–EELS can also probe surface phonons with Δx in the above ranges [8,16], similarly to other vibrational spectroscopy methods for surfaces, such as inelastic electron tunneling spectroscopy ($\Delta x \sim 0.1$ nm) [17], nano Raman spectroscopy ($\Delta x \sim 10$ nm) [18,19], angle-resolved photoemission spectroscopy ($\Delta x \sim 10^2$–10^3 nm) [20], and reflection EELS ($\Delta x \sim 10^3$ nm) [21]. Thus STEM–EELS is a unique tool for measuring phonon dispersions inside solids and surfaces at nanometer scales.

Although Senga *et al.* demonstrated that phonon dispersions are measurable for the nonpolar material of thin graphite (<7 nm) using a large scattering vector **q** [13], it remains unclear whether dispersions are measurable for thicker nonpolar crystals because of increased diffraction intensities. In addition, there have been no reports of quantitative measurements of scattering probability using phonon excitations in STEM–EELS for nonpolar or polar materials. In particular, diamond and c-BN are essential nonpolar and polar materials, respectively, with very high thermal conductivities for heat dissipation. By comparing diamond and c-BN using STEM–EELS, we can investigate the differences between polar and nonpolar crystals because of their similarities in crystal structure, hardness, heat conductivity, and so forth.

In this study, we used high-quality diamond and c-BN single crystals that form an epitaxial (111) heterointerface to conduct STEM–EELS measurements under exactly the same conditions, i.e., monochromaticity and current density of the electron probe, crystallographic orientation, and specimen thickness (Fig. S1) [22]. We measured the phonon dispersion of diamond (nonpolar) and its counterpart c-BN (polar), both with a thickness of $\sim$70 nm, using the large-**q** strategy in STEM–EELS with a nanometer-sized probe. To perform high-energy/high-spatial-resolution measurements, we used a monochromated electron nanoprobe for spectroscopy and a high-sensitivity scintillator for counting inelastically scattered electrons. By counting excited phonons, we evaluated the differential scattering cross sections $d\sigma/d\Omega$ of each phonon mode, i.e., transverse optical (TO), transverse acoustic (TA), longitudinal optical (LO), and longitudinal acoustic (LA) modes, for diamond and c-BN.
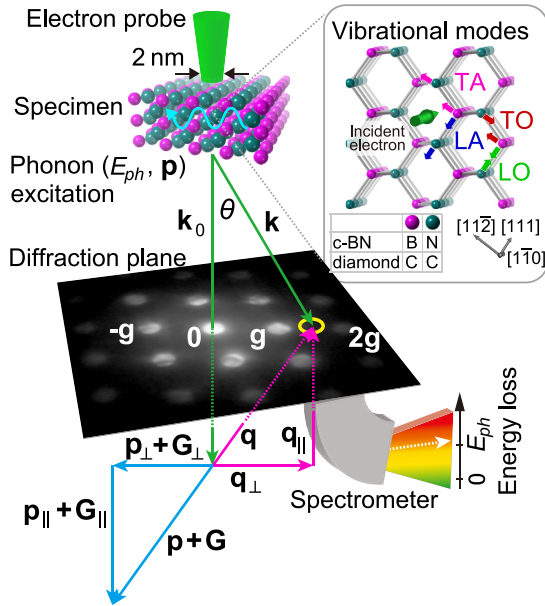
*kikkawa.jun@nims.go.jp

FIG. 1. Phonon spectroscopy principle. An incident electron with wave vector $\mathbf{k}_0$ excites a phonon with energy E_{ph} and wave vector $\mathbf{p}$, and is scattered with scattering vector $\mathbf{q}$ and then collected with a circular aperture located on the diffraction plane. A collected electron passing through a spectrometer is counted as one electron with energy loss E_{ph}. All vectors are divided into vertical and parallel components. From $-\mathbf{q}_\perp = \mathbf{p}_\perp + \mathbf{G}_\perp$, we can obtain the $\mathbf{p}_\perp$ vs E_{ph} relationship by changing the acceptable $\mathbf{q}_\perp$ with the circular aperture.

Phonon spectroscopy principle. Figure 1 shows the principle of phonon spectroscopy based on STEM–EELS using a nanometer-sized electron probe. Fast incident electrons with wave vector $\mathbf{k}_0$ and energy E_0 are scattered either elastically or inelastically in the specimen. $\mathbf{k}_0$ is set to be parallel to the $[1\bar{1}0]$ direction for diamond and c-BN. Most of the elastically scattered electrons contribute to the formation of spots at reciprocal lattice points on the diffraction plane such as $\mathbf{G} = 0$, $\pm\mathbf{g}$, and $\pm 2\mathbf{g}$. $\mathbf{g}_{111}$ and its magnitude are denoted as $\mathbf{g}$ and g, respectively, for simplicity throughout this paper. For an inelastically scattered electron with wave vector $\mathbf{k}$ that excites a single phonon, the conservation of momentum gives $-\mathbf{q} = \mathbf{p} + \mathbf{G}$, where $\mathbf{q}$ ($= \mathbf{k} - \mathbf{k}_0$) and $\mathbf{p}$ are the scattering vector and phonon wave vector defined in the first Brillouin zone (FBZ), respectively. The vectors are decomposed in the directions parallel and perpendicular to $\mathbf{k}_0$, as respectively denoted by the subscripts $\parallel$ and $\perp$. EELS for $\mathbf{q}_\perp$, i.e., $\mathbf{p}_\perp$, is carried out by locating the center of a wave-vector-selected aperture (yellow circle in Fig. 1) at $\mathbf{q}_\perp$ [see Methods, Figs. S2(a) and S2(b)]. When $q_\perp \ll k_0$, we can estimate $q_\parallel$ as $k_0 E_{ph}/2E_0 = 1.6 \times 10^{-3}$ nm^{-1} for $E_0 = 80$ keV and phonon energy $E_{ph} = 160$ meV [23,24]. Because $q_\parallel \ll g/2$, corresponding to the L point in the FBZ (15 nm^{-1} for diamond and c-BN), we can obtain the $\mathbf{p}_\perp$ vs E_{ph} relationship throughout the $\mathbf{q}_\perp$-dependent EELS. Excited phonons are counted using the conversion efficiency of the charge-coupled device (CCD) camera.

Dipole scattering for nonpolar and polar crystals. First, we demonstrate the difference in EELS spectra for dipole scattering, i.e., $\mathbf{q}_\perp = 0$ between nonpolar (diamond) and polar (c-BN) crystals in Fig. 2(a), only in this case, a wave-vector-

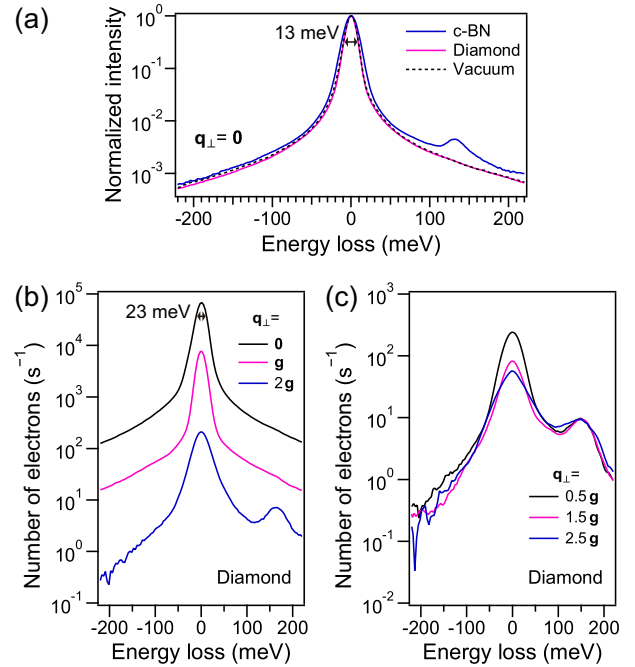FIG. 2. Phonon intensities in EELS. (a) EELS spectra for diamond, c-BN, and vacuum with $\mathbf{q}_\perp = 0$ and $\beta = 0.0039g$. EELS spectra acquired with (b) $\mathbf{q}_\perp = 0$, $\mathbf{g}$, and $2\mathbf{g}$ (Γ points) and (c) $\mathbf{q}_\perp = 0.5\mathbf{g}$, $1.5\mathbf{g}$, and $2.5\mathbf{g}$ (L points) for diamond using $\beta = 0.15g$, plotted as electron counts per second.

selected radius of $\beta = 1.2$ nm^{-1} (i.e., $0.0039g$) and a broader electron probe were used to satisfy the $\beta \to 0$ condition [Fig. S2(c)]. The peak intensity of $\sim 1/200$ of the zero-loss peak (ZLP) intensity at 131 meV and the small peak-shoulder intensity of around 160 meV for c-BN were assigned to the TO and LO phonons, respectively, whereas the intensity profile of the degenerated TO+LO mode for diamond was invisible and similar to the profile acquired in vacuum. This indicates that the EELS intensity of optical phonons for nonpolar crystals was very low relative to the elastic peak, i.e., ZLP.

Impact scattering with large scattering vector. Returning to the practical 2-nm probe mode (Fig. 1), we applied a large $\mathbf{q}_\perp$ [13] to diamond. Figures 2(b) and 2(c) show EELS spectra acquired at $\mathbf{q}_\perp = 0$, $\mathbf{g}$, and $2\mathbf{g}$ (Γ points) and $\mathbf{q}_\perp = 0.5\mathbf{g}$, $1.5\mathbf{g}$, and $2.5\mathbf{g}$ (L points), respectively, for diamond [Fig. S2(d)]. The TO+LO modes at Γ points, which are invisible at $\mathbf{q}_\perp = 0$ again, are slightly visible at $\mathbf{q}_\perp = \mathbf{g}$ and clearly visible at $\mathbf{q}_\perp = 2\mathbf{g}$ in Fig. 2(b), whereas the TO and LO modes at L points are clearly observed via their overlapping peaks at around 155 meV from the FBZ, i.e., $\mathbf{q}_\perp = 0.5\mathbf{g}$ in Fig. 2(c). Notably, the peak intensities of the TO+LO modes for $\mathbf{q}_\perp = 0.5\mathbf{g}$, $1.5\mathbf{g}$, and $2.5\mathbf{g}$ are invariable and approximately equivalent to that for $\mathbf{q}_\perp = 2\mathbf{g}$. This result suggests that the $\mathbf{q}_\perp$ dependence of the EELS intensity for TO+LO modes is small, presumably over the range $0 \leqslant \mathbf{q}_\perp \leqslant 2.5\mathbf{g}$ for diamond. Then the TO+LO modes become visible by reducing the ZLP tail intensity at ~ 160 meV to ~ 10 counts per second in Fig. 2(b) using a larger $\mathbf{q}_\perp$. In other words, the half width at 10^{-4} maximum (HWTTM) is required to be less than ~ 160 meV for the ZLP at $\mathbf{q}_\perp = 0$: HWTTM = ~ 1 eV in Fig. 2(b). The use of impact scattering
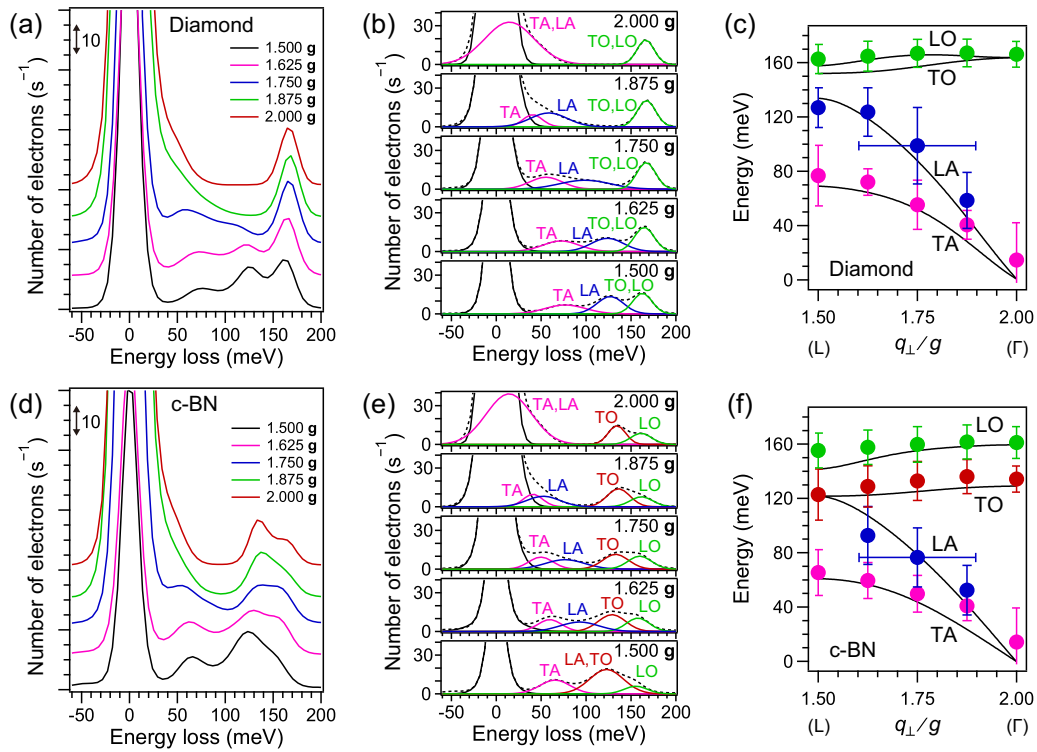
FIG. 3. Phonon dispersion measurements. (a) Deconvolved EELS spectra for diamond from 1.5**g** to 2**g** and (b) their multiple Gaussian fits. (c) Plot of phonon modes identified in (b) with the reference dispersion curve between the L and Γ points for diamond [27]. (d) Deconvolved EELS spectra for c-BN from 1.5**g** to 2**g** and (e) their multiple Gaussian fits. (f) Plot of phonon modes identified in (e) with the reference dispersion curve between the L and Γ points for c-BN [28]. Vertical error bars denote the FWHM of Gaussian profiles, whereas lateral error bars denote the wave-vector resolution, ± 4.5 nm^{-1}($= \pm 0.15$ g) (see Fig. S2).

with a larger $\mathbf{q}_\perp$ is advantageous for phonon detection as well as high spatial resolution, which is in contrast to a smaller $\mathbf{q}_\perp$ including dipole scattering with $\mathbf{q}_\perp = \mathbf{0}$, where phonon signals are invisible and delocalized [7]. Regarding the use of a larger $\mathbf{q}_\perp$, a longer exposure time (20–80 ms) was required to obtain higher signal-to-noise ratios, which degrades the energy resolution (FWHM of the ZLP), mainly due to the ZLP fluctuation originating from the slight instability of the STEM–EELS system. To recover the energy resolution, Richardson–Lucy deconvolution (RLD) [25,26] was applied using a kernel, i.e., the ZLP (FWHM 21 meV) acquired with a short exposure time, 0.1 ms, in vacuum (Fig. S3). It was confirmed that the intensity profiles between 0 and 200 meV after RLD are not artifacts.

Phonon dispersion measurements. Figures 3(a) and 3(d), respectively, show EELS spectra for single-crystal diamond and c-BN, acquired in the $\mathbf{q}_\perp$ range from 1.5**g** (L point) to 2**g** (Γ point) and processed using RLD (Fig. S3). Figures 3(b) and 3(e) show the intensity profile of each component in Figs. 3(a) and 3(d), respectively, using multiple Gaussian fits: a combination of two Gaussian profiles is effective for the ZLP. Because the vertical axis represents electron counts per second in Figs. 3(b) and 3(e), the area of the Gaussian profile for each phonon mode corresponds to the phonon counts per second, assuming a single scattering process, i.e., one phonon is created by a single electron. This means that, for example, in diamond, one optical phonon (either TO or LO mode) is excited per $\sim 10^5$ incident electrons under each

$\mathbf{q}_\perp$ condition. This is calculated as a more general physical quantity, $d\sigma/d\Omega$, later. Figures 3(c) and 3(f) show plots of the Gaussian center (i.e., energy) with the wave vector for all profile components except for the ZLP in Figs. 3(b) and 3(e), respectively, with reference dispersion curves (solid lines) for diamond [27] and c-BN [28]. All components can be clearly assigned to LO, TO, LA, and TA modes or their combination, for example, LO and TO for diamond, because the small LO–TO energy gap of $\lesssim 10$ meV (0 at Γ) [29] was not resolved in this experiment. For c-BN, the LO–TO gap of 20 (at L) to 30 (at Γ) meV is large, reflecting polar effects [30,31], and was resolved. The error bars in the energy for acoustic modes are larger than those for optical modes because of their larger and smaller dispersion gradients within the effective wave-vector-selected area [Fig. S2(a)] [23,32]. The good agreement between the dispersion plots experimentally obtained using a ~ 1-nm-radius electron probe and the reference dispersion curves in Figs. 3(c) and 3(f) demonstrate that phonon dispersion and its related properties can be measured at the nanometer scale.

Phonon mode mapping. By scanning the electron nanoprobe across the c-BN/diamond (111) heterointerface and conducting EELS at each probe position, we obtained phonon mode maps at the nanometer scale. The c-BN/diamond boundary in the scanning area in the low-angle annular dark-field (LAADF)−STEM image [Fig. 4(a)] is shifted from (i) to (ii) with an uncertain boundary area [i.e., the area where (i) faces (ii) indicated by double arrows], where
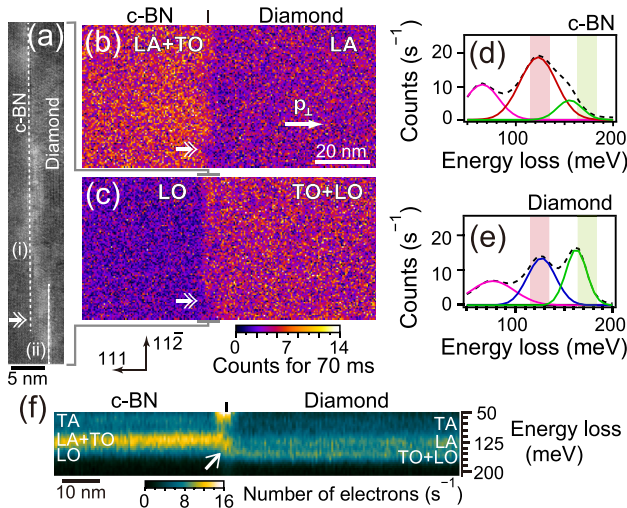
FIG. 4. Nanometric phonon mode mapping. (a) LAADF−STEM image at the c-BN/diamond interface. The interface shifts from (i) to (ii) with an uncertain boundary area (indicated by the double arrow). (b, c) Phonon counts maps across the c-BN/diamond interface obtained with $\mathbf{q}_\perp = 1.5\mathbf{g}$ (L point) and energy windows of (b) 115.1–136.0 meV and (c) 162.1–183.0 meV, respectively, as indicated in (d) for c-BN and (e) for diamond [enlargements of Figs. 3(b) and 3(e)]. Phonon counts of (b) LA+TO (c-BN) and LA (diamond) modes and (c) LO (c-BN) and TO+LO (diamond) modes are displayed. The single and double arrows denote the direction of phonon wave vector $\mathbf{p}_\perp$ (i.e., $[\bar{1}\bar{1}\bar{1}]$ direction) and the uncertain boundary area in Fig. 4(a), respectively. (f) Map of EELS spectra from c-BN to diamond areas across interface (i) [Fig. 4(a)] with $\mathbf{q}_\perp = 1.5\mathbf{g}$. The arrow denotes the vibration mode localized at the interface.

the additional contrast (bright area) arising from strain fields around the interface is visible (see also Fig. S4). Figures 4(b) and 4(c) show maps of phonon counts integrated in the ranges of 115.4–136.0 meV and 162.1–183.0 meV, respectively, for $\mathbf{q}_\perp = 1.5\mathbf{g}$ (i.e., L point) as indicated in Figs. 4(d) and 4(e) [enlargements of Figs. 3(b) and 3(e)], where the counting time, i.e., EELS acquisition time, was 70 ms at each pixel. The phonon modes that mainly contribute to counting are LA+TO and LA in the c-BN and diamond areas, respectively, in Fig. 4(a) and LO and TO+LO in the c-BN and diamond areas, respectively, in Fig. 4(b). All observed phonons propagate along the $[\bar{1}\bar{1}\bar{1}]$ direction. The mean and standard deviation of the phonon counts are 4.7 ± 2.2 (c-BN) and 3.2 ± 1.8 (diamond) in Fig. 4(a) and 1.5 ± 1.2 (c-BN) and 2.9 ± 1.7 (diamond) in Fig. 4(b). The c-BN/diamond boundary shape observed using optical phonons [Fig. 4(c)] is different from that observed using acoustic phonons [Fig. 4(b)], especially in the uncertain boundary area indicated by double arrows in Figs. 4(a)–4(c). The boundary profile (dotted line) shape in Fig. 4(a) is more similar to the boundary shape in Fig. 4(c) than that in Fig. 4(b), suggesting that vibrational energy is modulated at the interface in Fig. 4(b). Figure 4(f) shows the EELS map in the area, including the c-BN/diamond interface (i) [Figs. S5(a)–S5(c)]. A vibrational mode of 130 meV is observed at the interface as indicated by the arrow in Fig. 4(f). This mode is not interpreted to be a linear combination of EELS intensity profiles for c-BN and diamond at the L point [Fig. S5(d)], suggesting the presence of a vibrational mode
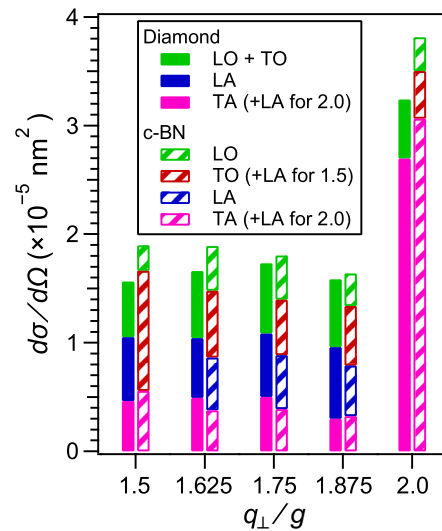

FIG. 5. Differential scattering cross sections. Stacked plots of the cross section $d\sigma/d\Omega$ of each phonon mode for diamond (solid bars) and c-BN (hatched bars). For phonon modes that are difficult to separate or inherently degenerate, the sum of $d\sigma/d\Omega$ values is used: LO+TO from 1.5 to 2.0 and TA+LA at 2.0 in $q_\perp/g$ for diamond and TO+LA at 1.5 and TA+LA at 2.0 in $q_\perp/g$ for c-BN.

localized at the interface. The results [Figs. 4(b), 4(c), and 4(f)] also demonstrate that the spatial resolution in phonon mapping is ∼2 nm (i.e., probe diameter) without fatal delocalization in the meV-range EELS owing to the use of large $\mathbf{q}_\perp$. It is notable that STEM–EELS enables the nanometric acoustic-phonon mapping and observation of the localized vibrational mode, which are difficult using optical probes.

Differential scattering cross section of phonon excitation. On the basis of Figs. 3(b) and 3(e), the differential cross section $d\sigma/d\Omega = \Delta N/(J_0 \, \Delta\Omega \, n_a)$ was calculated for each phonon mode and is plotted by stacking the results to obtain the cross sections for total phonon modes, i.e., TO, TA, LO, and LA modes, in Fig. 5. ΔN is the phonon counts per second, i.e., the Gaussian profile areas in Figs. 3(b) and 3(e), J_0 is the electron flux density (9.1×10^6 electrons s^{-1} nm^{-2}), and $\Delta\Omega$ is a small solid angle (2.9×10^{-5} sr). n_a is the number of atoms in the volume $\pi r^2 t$ and is estimated as 6.0×10^4 (diamond) and 5.8×10^4 (c-BN) using densities ρ of 3.52 and 3.487 g cm^{-3} for diamond and c-BN, where r and t are the electron probe radius (1 nm) and specimen thickness in the measured area (73 nm for diamond and 71 nm for c-BN), respectively. The $\mathbf{q}_\perp$ dependence of $d\sigma/d\Omega$ for the total phonon modes, i.e., the plot maximum, is similar for diamond and c-BN in the range $1.5 \leqslant q_\perp/g \leqslant 2.0$. $d\sigma/d\Omega$ values for the total phonon modes are 1.5–1.7 $\times 10^{-5}$ nm^2 (diamond) and 1.6–1.9 $\times 10^{-5}$ nm^2 (c-BN) for $1.5 \leqslant q_\perp/g \leqslant 1.875$, which are approximately twice those at $q_\perp/g = 2$. $d\sigma/d\Omega$ for each phonon mode appears to be constant, except for the increased $d\sigma/d\Omega$ of the acoustic (TA+LA) component at $q_\perp/g = 2$. Elastically scattered electrons forming the 2**g** diffraction disk can contribute to the increase in $d\sigma/d\Omega$ at $q_\perp/g = 2$.

Discussion. The mean free path of an 80-keV incident electron for phonon excitations, λ_{ph}, in diamond has been reported to be ∼1×10^3 nm [33,34]. Because the $d\sigma/d\Omega$ values are similar for diamond and c-BN (Fig. 5), λ_{ph} in

c-BN is also expected to be $\sim 1 \times 10^3$ nm. This means that an incident electron can excite a phonon once when passing through the diamond and c-BN crystals with a thickness of ~ 70 nm in this experiment. Actually, EELS intensities arising from double phonon scattering were not detected in this experiment. For diamond (nonpolar) crystals with a thickness much larger than ~ 70 nm, multiple electron diffraction increases the diffraction disk intensity at $2\mathbf{g}$ [35]; thus the optimal $\mathbf{q}_\perp$ can be larger than $2\mathbf{g}$ for phonon measurements at the Γ point. The phonon lifetimes τ of optical modes for diamond and c-BN are 2.9×10^{-12} and 1.7×10^{-12} s, respectively, at room temperature [36–38], and τ for the acoustic modes is likely to be larger than that for the optical modes [39]. Because an incident electron arrives every 3.5×10^{-8} s ($\gg \tau$) on average in this experiment, all the incident electrons interact with the relaxed lattice system. Regarding the width of the Gaussian fits in Fig. 3, the FWHM for the LO phonon of c-BN, for example, is 29.6 ± 1.1 meV for $1.5 \leqslant q_\perp/g \leqslant 2.0$. From the uncertainty relation, the energy spread h/τ is estimated as 2.4 meV for the LO mode of c-BN with $\tau = 1.7 \times 10^{-12}$ s [37,38], where $h = 4.136 \times 10^{-12}$ meV/s is Planck's constant. This implies that the FWHM of each phonon mode for diamond and c-BN in Fig. 3 mainly reflects both the energy and wave-vector resolutions in this experiment: the energy range of each phonon mode in the measurement is determined by the wave-vector resolution through dispersions ($\mathbf{p}_\perp$ vs E_{ph}). An improvement of wave-vector resolution will reduce the FWHM of the acoustic modes, especially for a large phase velocity $dE_{\mathrm{ph}}/d\mathbf{p}_\perp$.

Conclusion. We measured the phonon dispersions of diamond and c-BN using STEM−EELS with a nanometer-sized electron probe and large scattering vectors, and demonstrated phonon mode mapping at the c-BN/diamond interface. We quantitatively evaluated differential scattering cross sections for excitations of each phonon mode. The use of large scattering vectors is critical for detecting phonons at high spatial resolutions, especially in nonpolar crystals. This study has paved the way for experimental phonon analysis at heterointerfaces and lattice defects, which exist at the present c-BN/diamond interface [Figs. 4(a), S1(c), and S5] [40], regardless of their polarity.

Methods. A high-quality c-BN single crystal was epitaxially grown on the (111) surface of a single-crystal diamond seed at 5.5 GPa and 1500 °C [Fig. S1(a)] using the temperature gradient method and a modified belt-type high-pressure apparatus (FB60H) [41,42]. Hexagonal BN and lithium boron nitride (Li_3BN_2) were used as the source and solvent, respectively. Specimens for EELS were prepared using a focused ion beam (FIB) (Scios 2 and Helios G4, Thermo Fisher Scientific, Inc.) [Fig. S1(b)]. A monochromated electron microscope (Themis Z, Thermo Fisher Scientific, Inc.) with a spectrom-

eter (Quantum 970, Gatan Inc.) was used for STEM–EELS. To obtain the spectra in Figs. 2(b), 2(c), and 3, an 80-keV electron probe with a diameter of 2 nm, a convergence semi-angle of 3.2 mrad ($= 4.8$ nm^{-1}), and a beam current of 4.6 pA ($= 2.9 \times 10^7$ electrons s^{-1}) was scanned in areas of diamond and c-BN ~ 40 nm from the heterointerface [Fig. S1(c)]. The electron incident direction was set as the [1$\bar{1}$0] direction for both materials. Using a 1-mmφ aperture with collection radius $\beta = 3.0$ mrad ($= 4.5$ nm^{-1}) and relatively shifting its center position $\mathbf{q}_\perp$ along the [111] direction (i.e., $\mathbf{g}_{111}$ direction) on the diffraction plane [Figs. 1 and S2(d)], we recorded inelastic electrons with specific wave vectors [Figs. S2(a) and S2(b)] using a CCD camera with a high-sensitivity scintillator (994 US1000XP U$^+$, Gatan Inc.). The exposure time at every dwell point was set at 5 ms for $\mathbf{q}_\perp = \mathbf{0}$ and 20–80 ms for $0.5\mathbf{g} \leqslant \mathbf{q}_\perp \leqslant 2.5\mathbf{g}$. A single EELS spectrum was obtained after ZLP alignment for all 4000 spectra; subsequently, their sum was obtained. Figures 4(b)–4(d) were simultaneously obtained by scanning the nanoprobe across the c-BN/diamond (111) heterointerface using the same experimental condition as for $\mathbf{q}_\perp = 1.5\mathbf{g}$ mentioned above. The scanning step and exposure time were 0.5 nm and 70 ms per pixel, respectively. The energy dispersion of the spectrometer was determined to be 3.84 meV/ch for EELS in Figs. 2(a) and 2(b) and 5.23 meV/ch for EELS in Figs. 3 and 4. In the case of a weak ZLP, an energy dispersion of 5.23 meV/ch was found to be efficient for obtaining a higher signal-to-noise ratio in the spectra. To obtain the spectra in Fig. 2(a), we used a 30-keV parallel beam with a diameter of ~ 400 nm, $\beta = 0.9$ mrad ($=1.2$ nm^{-1}), and an energy dispersion of 1.90 meV/ch [Fig. S2(c)]. The FWHMs of the raw ZLP were 13–20 meV, 23–38 meV, 42–54 meV, and 31–37 meV for the spectra in Figs. 2(a)–2(c) and 3, respectively. The conversion efficiencies of the CCD were 27.6 and 11.3 counts per electron collision for 80 and 30 keV, respectively. The specimen was kept at room temperature throughout this study. The ZLP at vacuum for RLD, i.e., the kernel, was obtained after the ZLP alignment for all 10 000 spectra recorded with a shorter exposure time of 0.1 ms. The FWHM of this ZLP (kernel) for 80 keV was 21 meV. To determine the thickness of the measurement areas for diamond and c-BN, EELS spectra including plasmons were acquired with an energy dispersion of 0.05 eV/ch (Fig. S6). The thickness was calculated to be 73 and 71 nm for diamond and c-BN, respectively, using the standard log-ratio method (Fig. S6) [23]. The LAADF−STEM image in Fig. 4(a) was taken with 300-keV electrons and a collection semiangle range of 12–47 mrad.

[1] A. L. Moore and L. Shi, Mater. Today **17**, 163 (2014).

[2] D. G. Cahill, W. K. Ford, K. E. Goodson, G. D. Mahan, A. Majumdar, H. J. Maris, R. Merlin, and S. R. Phillpot, J. Appl. Phys. **93**, 793 (2003).

[3] H. Song, J. Liu, B. Liu, J. Wu, H.-M. Cheng, and F. Kang, Joule **2**, 442 (2018).

[4] K. Biswas, J. He, I. D. Blum, C.-I. Wu, T. P. Hogan, D. N. Seidman, V. P. Dravid, and M. G. Kanatzidis, Nature (London) **489**, 414 (2012).

[5] S. I. Kim, K. H. Lee, H. A. Mun, H. S. Kim, S. W. Hwan, J. W. Roh, D. J. Yang, W. H. Shin, X. S. Li, Y. H. Lee, G. J. Snyder, and S. W. Kim, Science **348**, 109 (2015).

[6] O. L. Krivanek, T. C. Lovejoy, N. Dellby, T. Aoki, R. W. Carpenter, P. Rez, E. Soignard, J. Zhu, P. E. Batson, M. J. Lagos, R. F. Egerton, and P. A. Crozier, Nature (London) **514**, 209 (2014).

[7] C. Dwyer, T. Aoki, P. Rez, S. L. Y. Chang, T. C. Lovejoy, and O. L. Krivanek, Phys. Rev. Lett. **117**, 256101 (2016).

[8] M. J. Lagos, A. Trügler, U. Hohenester, and P. E. Batson, Nature (London) **543**, 529 (2017).

[9] F. S. Hage, D. M. Kepaptsoglou, Q. M. Ramasse, and L. J. Allen, Phys. Rev. Lett. **122**, 016103 (2019).

[10] F. S. Hage, G. Radtke, D. M. Kepaptsoglou, M. Lazzeri, and Q. M. Ramasse, Science **367**, 1124 (2020).

[11] E. Burkel, Rep. Prog. Phys. **63**, 171 (2000).

[12] F. S. Hage, R. J. Nicholls, J. R. Yates, D. G. McCulloch, T. C. Lovejoy, N. Dellby, O. L. Krivanek, K. Refson, and Q. M. Ramasse, Sci. Adv. **4**, eaar7495 (2018).

[13] R. Senga, K. Suenaga, P. Barone, S. Morishita, F. Mauri, and T. Pichler, Nature (London) **573**, 247 (2019).

[14] J. C. Idrobo, A. R. Lupini, T. Feng, R. R. Unocic, F. S.Walden, D. S. Gardiner, T. C. Lovejoy, N. Dellby, S. T. Pantelides, and O. L. Krivanek, Phys. Rev. Lett. **120**, 095901 (2018).

[15] M. J. Lagos and P. E. Batson, Nano Lett. **18**, 4556 (2018).

[16] H. Lourenço-Martins and M. Kociak, Phys. Rev. X **7**, 041059 (2017).

[17] L. J. Lauhon and W. Ho, Phys. Rev. B **60**, R8525 (1999).

[18] R. P. V. Duyne, J. C. Hulteen, and D. A. Treichel, J. Chem. Phys. **99**, 2101 (1993).

[19] A. Hartschuh, E. J. Sánchez, X. S. Xie, and L. Novotny, Phys. Rev. Lett. **90**, 095503 (2003).

[20] C. Chen, J. Avila, S. Wang, Y. Wang, M. Mucha-Kruczyński, C. Shen, R. Yang, B. Nosarzewski, T. P. Devereaux, G. Zhang, and M. C. Asensio, Nano Lett. **18**, 1082 (2018).

[21] C. Oshima, T. Aizawa, R. Souda, Y. Ishizawa, and Y. Sumiyoshi, Solid State Commun. **65**, 1601 (1988).

[22] See Supplemental Material at http://link.aps.org/supplemental/10.1103/PhysRevB.104.L201402 for the specimen, wave-vector selection, RLD process, and phonon analysis at the heterointerface.

[23] R. F. Egerton, *Electron Energy-Loss Spectroscopy in the Electron Microscope*, 3rd ed. (Springer, New York, 2011).

[24] J. Kikkawa, T. Mizoguchi, M. Arai, T. Nagai, and K. Kimoto, Phys. Rev. B **98**, 075103 (2018).

[25] W. H. Richards, J. Opt. Soc. Am. **62**, 55 (1972).

[26] L. B. Lucy, Astron. J. **79**, 745 (1974).

[27] P. Pavone, K. Karch, O. Schütt, W. Windl, D. Strauch, P. Giannozzi, and S. Baroni, Phys. Rev. B **48**, 3156 (1993).

[28] K. Karch and F. Bechstedt, Phys. Rev. B **56**, 7404 (1997).

[29] J. L. Warren, J. L. Yarnell, G. Dolling, and R. A. Cowley, Phys. Rev. **158**, 805 (1967).

[30] S. Mukhopadhyay and D. A. Stewart, Phys. Rev. Lett. **113**, 025901 (2014).

[31] S. Adachi, *Optical Properties of Crystalline and Amorphous Semiconductors* (Springer, Boston, 1999).

[32] H. Kohl, Ultramicroscopy **16**, 265 (1985).

[33] L. J. Allen and C. J. Rossouw, Phys. Rev. B **42**, 11644 (1990).

[34] G. Radi, Acta Cryst. A **26**, 41 (1970).

[35] P. B. Hirsch, R. B. Nicholson, A. Howie, D. W. Pashley, and M. J. Whelan, *Electron Microscopy of Thin Crystals* (Butterworths, London, 1965).

[36] A. Laubereau, D. von der Linde, and W. Kaiser, Phys. Rev. Lett. **27**, 802 (1971).

[37] A. I. Lukomskii, V. B. Shipilo, E. M. Shishonok, and N. G. Anichenko, Phys. Status Solidi A **102**, K137 (1987).

[38] G. P. Srivastava, J. Phys.: Condens. Matter **21**, 174205 (2009).

[39] G. Nilsson and G. Nelin, Phys. Rev. B **3**, 364 (1971).

[40] C. Chen, Z. Wang, T. Kato, N. Shibata, T. Taniguchi, and Y. Ikuhara, Nat. Commun. **6**, 6327 (2015).

[41] T. Taniguchi, J. Ceram. Soc. Jpn. **128**, 620 (2020).

[42] T. Taniguchi and S. Yamaoka, Mater. Res. Soc. Symp. Proc. **472**, 379 (1997).